PHYSICAL REVIEW E **81**, 046308 (2010)

Liquid-phase continuity and solute concentration dynamics during evaporation from porous media: Pore-scale processes near vaporization surface

N. Shokri,[*] P. Lehmann, and D. Or

Soil and Terrestrial Environmental Physics, Department of Environmental Sciences, Swiss Federal Institute of Technology Zurich, Zurich, Switzerland

(Received 26 January 2010; published 13 April 2010)

Evaporation from porous media involves complex pore scale transport processes affecting liquid phase distribution and fluxes. Often, the initial evaporation rate is nearly constant and supplied by capillary flow from wetted zones below to the surface. Sustaining constant flow against gravity hinges on an upward capillary gradient and on liquid phase continuity with hydraulic conductivity sufficient for supplying evaporative flux. The pore scale liquid phase adjustments during evaporative displacement necessary for maintaining a constant flux have been postulated but rarely measured. In this study we employed detailed imaging using x-ray synchrotron radiation to study liquid phase distribution and dynamics at the most sensitive domain just below the surface of evaporating sand columns. Three-dimensional images at a resolution of 7 microns were obtained from sand column (mean particle size 0.6 mm) initially saturated with calcium iodide solution (4% by mass) to enhance image contrast. Detailed imaging of near-surface liquid phase distribution during evaporation confirmed phase continuity at micrometric scale and provided quantitative estimates of liquid conductance in agreement with values required to supply evaporative flux. Temporal variations in bulk salt concentrations determined from x-ray attenuation were proportional to evaporative water mass loss. Highly resolved salt concentration images revealed existence of evaporating chimneys that supply the bulk of evaporative demand. Delineated mass loss dynamics and salt distribution measured by the x-ray attenuation were in reasonable agreement with a simplified analytical convection-diffusion model for salt dynamics during evaporation from porous media.

DOI: 10.1103/PhysRevE.81.046308 PACS number(s): 47.56.+r

I. INTRODUCTION

Evaporation from porous media is a common process important for many environmental and industrial applications such as drying of foods and building materials and hydrological processes such as evapotranspiration. Evaporation from soil affects energy balance, land surface-atmosphere interactions, and agricultural water management and influences many biological activities in the vadose zone. Most evaporation processes from porous media can be viewed as an immiscible displacement process [1] where less viscous nonwetting fluid (air) displaces a more viscous wetting fluid (water) occupying the pore space where the dynamic interface between wet and partially dry zones is known as the drying front. Typically, two stages are distinguished, an initial regime in which evaporation rate is relatively high and nearly constant, so-called stage 1 evaporation, limited primarily by atmospheric conditions and supplied by capillary liquid flow connecting a receding drying front with an evaporating surface [2–5]. At a certain drying front depth deduced from pore size distribution [4], continuous liquid pathways are interrupted when gravity and viscous effects overcome capillary forces. Interruption of the continuous liquid pathways marks the onset of a new evaporation regime with lower evaporation rate limited by transport properties of porous media, the so-called stage 2 evaporation [6].

Maintenance of continuous capillary liquid pathways while a drying front recedes into the porous medium is key to understanding evaporation behavior and associated pore scale mass transport mechanisms. In a series of two-dimensional experiments, Shaw [1] illustrated that the drying patterns could be analyzed by invasion percolation and concluded that liquid film flow within crevices and particle contacts plays a significant role in drying behavior. Shaw's experiments were followed by extensive modeling work [3]; most postulated existence of capillary induced liquid flow as also supported by experimental studies illustrating the dominant role of continuous liquid pathways on evaporation behavior [4–11]. Despite valuable insights gained from past experimental and theoretical studies, quantitative analysis of pore scale liquid continuity dynamics during evaporation is rare due to observational challenges confounded by complexity of pore spaces. Moreover, direct experimental evidence regarding the structure and hydraulic capacity of liquid films for supplying evaporative demand remain inconclusive.

In addition to quantification of evaporation behavior, understanding dynamics of continuous liquid pathways is important for delineating evolution of salt deposition and concentration distribution during evaporation from porous media [12,13]. Links between salt dynamics and evaporation are important for various environmental and engineering applications such as crops in arid areas, surface water quality, biodiversity, and microbiological activity in the vadose zone. The geometry and dynamics of continuous liquid pathways define convective salt transport and deposition at evaporating surfaces. Hence, solutes may be used as a tracer to directly establish the continuity of liquid films and delineate the location of vaporization zones during evaporation from porous media at pore scale.

---

[*] Present address: Department of Earth Sciences, Boston University, Boston, MA 02215, USA; nshokri@bu.edu

This study was motivated by the need to resolve details of liquid flow and phase distribution just below an evaporating surface and to assess the role of capillary film and corner flow in supplying evaporative flux. The specific objectives of the study were to: (1) observe and quantify dynamics of continuous liquid pathways during evaporation from porous media at pore scale, (2) quantify the contribution of the capillary liquid flow in supplying the total evaporative water loss, and (3) analyze patterns of salt concentration and deposition as markers for continuity and evaporation locations. Quantitative analysis of dynamics of salt distribution during evaporation from porous media received relatively little attention, with only a few studies addressing spatiotemporal evolution of salt concentration during evaporation [14,15]

II. THEORETICAL CONSIDERATIONS

A. Liquid flow in microscopic films and crevices in an angular capillary

Experimental evidence suggests that liquid fluxes at low water contents are supplied by capillary flows through liquid films and angular crevices [16–19]. Tuller and Or [17] presented a model to predict the mean liquid flow velocity in corners bounded by liquid-vapor interfaces as

$$v = \frac{r^2}{\varepsilon \eta_\circ}\left(-\frac{dp}{dz}\right), \tag{1}$$

where v is mean flow velocity, dp/dz is the pressure head gradient in flow direction z, $\eta_\circ$ is the dynamic viscosity, ε is the dimensionless flow resistance parameter that depends on corner angle, and r is the radius of liquid-vapor interface curvature defined by capillary pressure head, h, as

$$r = \frac{2\sigma}{\rho g h}, \tag{2}$$

with σ surface tension, ρ density, and gravity acceleration g. The flow resistance parameter was estimated by Tuller and Or [17] fitting a parametric expression to tabulated values of Ransohoff and Radke [18] as

$$\varepsilon = \exp\left(\frac{a + b\gamma}{1 + c\gamma}\right), \tag{3}$$

where $a=2.124$, $b=0.007\,83$, and $c=-0.004\,15$ and γ is the corner angle in the range of $10<\gamma<150°$. To compute cumulative water loss from an evaporating porous medium, the flux obtained by Eq. (1) must be adjusted to evaporating surface geometry. Tuller *et al.* [20] determined the wet cross-sectional area, A_w, in corners of a single pore of arbitrary polygonal cross section consisting of n sides as

$$A_w = r^2 \sum_{i=1}^{n}\left(\frac{1}{\tan(\gamma/2)} - \frac{\pi(180-\gamma)}{360}\right). \tag{4}$$

Using Eqs. (1)–(4), one can estimate liquid flux supplied by capillary flow through corners of an angular capillary. By comparing predicted hydraulic conductivity resulting from liquid flow in a representative angular capillary with measured experimental data of saturation and hydraulic conductivity of Hygiene sandstone, Tuller and Or [17] confirmed that liquid flow through a porous medium with narrow pore size distribution (e.g., sand) can be represented by flow through a single representative angular pore. A recent study by Chauvet *et al.* [21] demonstrated experimentally similarity between drying periods from a single capillary tube with square cross section with drying curve from porous media.

B. Spatiotemporal solute distribution during evaporation from porous media

During evaporation from porous media saturated with salt solution, dissolved salt is transported by convection induced by capillary liquid flow toward evaporating surface where it accumulates, whereas diffusion (Brownian motion) tends to spread the salt and homogenize concentrations in space [22]. The resulting interplay between convection and diffusion affects dynamics of salt distribution near an evaporating surface. The competition between diffusion and convection is often characterized by the dimensionless Peclet number, which for drying porous media is defined as [22]

$$\mathrm{Pe} = \frac{eL}{D^* \varphi}, \tag{5}$$

where e is the evaporation rate, L is the length of the column, D^* is the effective diffusion coefficient of the dissolved salt, and φ is the porosity. Based on the convection-diffusion equation, Huinink *et al.* [22] provided analytical tools to study transport behavior of salt during evaporation from porous media valid for times after the onset of drying process. Their approach was improved by Guglielmini *et al.* [12] providing an analytical solution characterizing the process over a longer time period. The main conclusion of these studies was that Peclet number is the key parameter to study dissolved-salt distribution during evaporation from porous media. While uniform salt distribution within porous medium occurred for $\mathrm{Pe} \ll 1$ (diffusion dominates convection), salt is mainly accumulated close to surface (where evaporation happens) when $\mathrm{Pe} \gg 1$ (capillary driven liquid flow dominates diffusion). The tempospatial dissolved-salt distribution during evaporation from porous media was studied numerically by solving the convection-diffusion equation (CDE) [12,22]. With some practical assumptions Guglielmini *et al.* [12] reduced the partial differential equation form of CDE to an ordinary differential equation (ODE) describing the dynamics of salt distribution during evaporation. The simplified ODE was solved analytically for intermediate times predicting spatiotemporal evolution of salt mass fraction for $\mathrm{Pe} \gg 1$ expressed as

$$\Omega(\xi,\tau) = 1 - \mathrm{Pe}\,\tau + \frac{\mathrm{Pe}^2 \tau \,\mathrm{Erfi}\left(\frac{\sqrt{\mathrm{Pe}}(\xi-1)}{\sqrt{2-2\mathrm{Pe}\,\tau}}\right)}{(\mathrm{Pe}\,\tau - 1)\,\mathrm{Erfi}\left(\frac{\sqrt{\mathrm{Pe}}}{\sqrt{2-2\mathrm{Pe}\,\tau}}\right)}, \tag{6}$$

where Erfi is the imaginary error function and $\Omega(\xi,\tau)$ is the normalized salt mass fraction defined as the ratio of salt mass

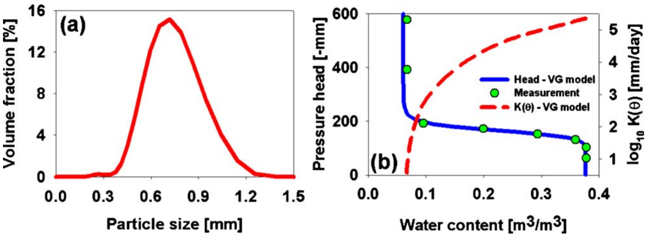

FIG. 1. (a) (Color online) Particle size distribution of sand used in the evaporation experiment determined by laser diffraction particle size analysis. (b) Relationship between capillary pressure and water content measured in the laboratory under hydrostatic conditions. The curve was fitted according to the parametric model of van Genuchten. The dashed line was determined with the unsaturated hydraulic conductivity model of van Genuchten [23] and Mualem [24]. Air-entry value of sand (applied pressure head to enable air invasion) was about 120 mm.

fraction at dimensionless depth ξ below surface to the salt mass fraction averaged over the entire domain, with ξ defined by $\xi = y/L$ and y is the depth below surface. The dimensionless time is defined as $\tau = tD^*/L^2$ where t is the elapsed time. The details of the derivation were explained in Guglielmini *et al.* [12].

Although the analytical solution in Eq. (6) was derived for a constant Peclet number during evaporation, Guglielmini *et al.* [12] found good agreement of the analytical solution with complete numerical results considering different Peclet numbers and times. In this study, we examine the applicability of Eq. (6) using experimental data obtained by means of x-ray synchrotron radiation during evaporation from sand column saturated with salt solution. Additionally, we plan to exploit pore scale observations of spatiotemporal patterns of solute concentration at the surface to identify regions with high and localized evaporative flux (denoted as "chimneys"). Solute dynamics and patterns are also useful for assessing continuous capillary connections and hydraulic conductance actively participating in supplying evaporation flux.

III. EXPERIMENTAL CONSIDERATION

To relate drying rates to spatial distribution of liquid phase at pore scale, a small sand column was scanned during evaporation using x rays from synchrotrons. Below we describe the physical properties of the porous medium and the imaging procedure.

A. Physical characterization of porous medium

A cylindrical column of 12 mm in height and 5 mm in diameter packed with hydrophilic sand (average particle size 0.6 mm) was used in the evaporation experiment. Sand particles were packed in column filled with calcium iodide solution (4% mass concentration). This solute was used to (i) study dynamics of salt distribution during evaporation from porous media and (ii) to enhance visual contrast between air, liquid and solid phases. Figure 1(a) depicts sand sample particle size distribution determined by laser diffraction particle size analyzer (LS 13 320 Multiwavelength Particle Size Analyzer, Beckman Coulter). The resulting packing porosity was 0.38 (averaged over entire column). The relation between water content θ and capillary pressure (in the following denoted as water retention curve) was determined in the laboratory and parametric model of van Genuchten [23] was fitted to data as presented in Fig. 1(b) and Table I. The unsaturated hydraulic conductivity, $K(\theta)$, was computed according to the model of van Genuchten [23] and Mualem [24] using parameters presented in Table I. Saturated hydraulic conductivity, K_s, for the sand was experimentally determined as $156\ \text{mm min}^{-1}$ [4].

TABLE I. Parameter values used for models of van Genuchten [23] and Mualem [24] with residual water content θ_{res}, saturated water content θ_{sat}, α is inverse of characteristic capillary pressure head, and n is related to width of pore size distribution.

θ_{sat}	θ_{res}	α (mm)	n	K_s (mm min^{-1})
0.38	0.06	0.0061	12.75	156

B. Pore-scale imaging

The drying experiment was conducted at the TOMCAT beamline of the Swiss Light Source (Paul Scherrer Institute, Villigen, Switzerland). At seven different time steps after onset of evaporation, the column was scanned with x-rays from synchrotrons. The height of the x-ray beam was about 2.66 mm and 1500 radiographies were recorded within 6 min to reconstruct three-dimensional density distribution with pixel size of 7 microns for a volume of 5 mm in diameter and 2.66 mm in height. To obtain phase distribution for the entire column height, the column was shifted after each scan resulting in four blocks, 2.66 mm in height each. Scanning time of the entire column was about 30 min. The scan of the entire column included 1520 reconstructed images of horizontal cross sections with gray values representing density distribution within the porous medium. To segment the image in solid, gas, and liquid phases, the gray value distribution of each cross section was used to determine threshold values separating the three phases. We used the image of the first time step to classify between grains and saturated pore spaces measured before air invaded pore spaces. For subsequent time steps with the partially saturated media, we applied another gray value to distinguish between the air and liquid in each cross section.

In subsequent analyses we neglected the sample's top 1 mm (140 cross sections) in which porosity was not well defined (transitioning from 100% porosity to mean value of 38%). For the remaining 1380 cross-sectional images, we determined the water content for each time step counting the number of image elements assigned to liquid phase and deduced the drying rate by change in liquid content between two scans.

IV. RESULTS AND DISCUSSIONS

A. Liquid-phase continuity

In the following we present pore scale spatial distributions of liquid phase measured at different times following onset

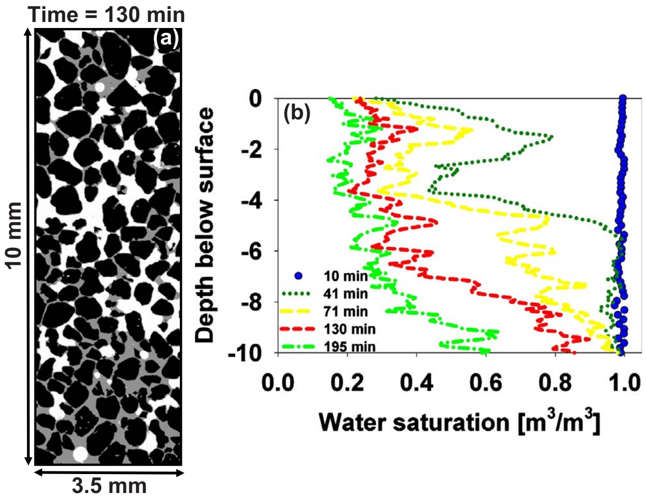

FIG. 2. (a) (Color online) Vertical cross section through three-dimensional reconstructed image of sand column scanned 130 min after onset of evaporation. The black, gray, and white colors correspond to the solid, liquid, and air phases, respectively. Evaporation occurs at top boundary and all other boundaries are closed. (b) Evolution of water content profile during evaporation. The drying front depth reaches 5 mm after 41 min and 9.2 mm after 71 min.

of evaporation experiment. An example of pore scale phase distribution in a vertical cross section during evaporation is shown in Fig. 2(a).

The vertical cross section indicates a water content gradient between bottom and top of column. More detailed information on water content distribution is shown in Fig. 2(b) and reveals that during evaporation the air phase penetrates deeper into the medium and the top surface gradually dries out. Although the gradual decrease of surface liquid content suggest presence of hydraulic connections between surface and wet regions below, a more direct verification of hydraulic continuity is shown in Fig. 3 for the top 1.7 mm of the sand column.

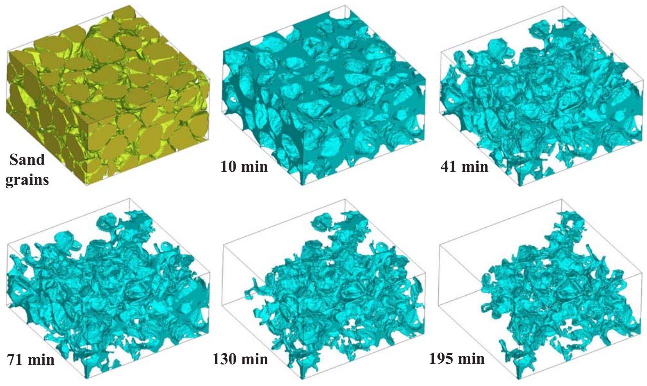

FIG. 3. (Color online) Liquid-phase distribution during evaporation from sand column using x rays from synchrotrons. The arrangement of sand grains and liquid phase within the first scanned block ($3.3 \times 3.3 \times 1.7$ mm^3) is shown for five time steps. Isolated liquid clusters were filtered out to highlight continuous liquid phase only. In course of evaporation, water content decreases without breaking phase continuity.

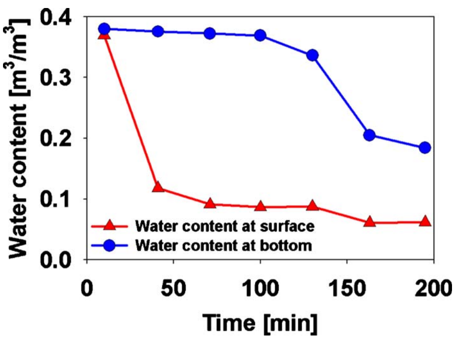

FIG. 4. (Color online) Temporal evolution of water content at surface and bottom of the sand column scanned seven times during evaporation experiment. Water content was computed from top and bottom images corresponding to depth difference of 10 mm. The difference in water contents corresponds to gradient in capillary pressure driving water flow toward the surface.

The three-dimensional liquid phase distribution presented in Fig. 3 indicated dynamics of the continuous liquid pathways within the first scanned block of the sand sample ($3.3 \times 3.3 \times 1.7$ mm^3). Just the continuous liquid paths extending from the surface to 1.7 mm below the surface of the sand column were illustrated in Fig. 3 and the isolated liquid clusters were filtered out. Despite the low water content close to the surface at the later stages of drying, liquid phase remained connected through the entire sand sample. These results prove the existence of the hydraulic connection and capillary liquid supply from wetted zone to the evaporation surface at microscale to meet the evaporative demand.

B. Capillary flow

We seek definitive insights regarding the question whether flow conductance in the most restrictive region below vaporization surface is sufficient to sustain observed drying rate. Upward capillary flow is determined by conductivity of liquid phase and a driving capillary pressure gradient. The hydraulic conductivity of partially saturated medium was estimated by two methods: as pore scale based corner flow model, and as macroscale sample averaged coefficient for Buckingham-Darcy [as seen in Fig. 1(b)]. For porous media with a narrow pore size distribution a representative unit angular capillary with corner flow model is sufficient to represent retention and capillary conduction in the medium [17]. The corner flow model [Eqs. (1)–(4)] requires estimation of interfacial curvature r at the corners which was obtained from the water characteristic curve (WCC) [Fig. 1(b)]. For a certain average liquid content θ in sample cross section, the corresponding capillary pressure head h was deduced from WCC [Fig. 1(b)] and Eq. (2) used to determine curvature r. The curvatures obtained from the cross-sectional images corresponding to the top and bottom of the sand column were determined according to this procedure and the average value r between surface and bottom (or position of drying front for first time steps) was used in Eqs. (1) and (4).

To assess vertical flow, the driving capillary pressure gradient must also be determined according to Eq. (1). Figure 4 illustrates the evolution of water content at the top and bot-

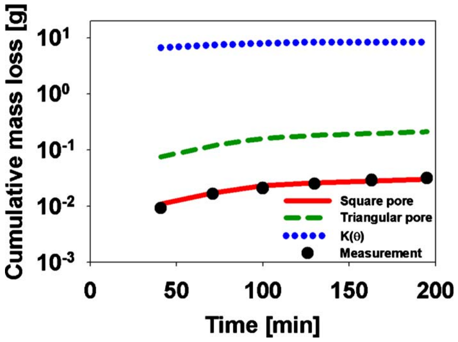

FIG. 5. (Color online) Cumulative water loss deduced from image analysis (measurement) compared to predictions with corner flow model (for pores with square and triangular cross section denoted by solid (red) and dashed (green) line, respectively) and the flux estimated using $K(\theta)$, the macroscopic hydraulic conductivity according to Buckingham-Darcy law. The models indicate that porous medium can sustain drying rate and is not limited by hydraulic properties.

tom of the sand column used to compute driving capillary pressure difference based on the water retention curve [Fig. 1(b)]. For the first four scans, liquid flows from the receding drying front (determined according to depth of longest continuous air pathway) to the surface with pressure at the front equal to air entry value [10]. In the last three scans, liquid flows from bottom of the column toward surface with pressure values estimated according to the water retention curve.

To use the corner flow model, we represent pore structure by angular capillaries with square cross section as was assumed in several previous studies [3,16,25]. Flow resistance parameter for square shape pore ($\gamma=90°$) is estimated from Eq. (3) as $\varepsilon=91$. Using Eq. (2), and considering parameter values $\sigma=0.0727\ \mathrm{kg\ s^{-2}}$, $\rho=1000\ \mathrm{kg\ m^{-3}}$, and $g=9.81\ \mathrm{m\ s^{-2}}$, computed liquid curvatures in different scans were in the range of 0.04 mm resulting in total wet area A_w at corners of single capillary tube with square cross section as $1.6\times10^{-3}\ \mathrm{mm}^2$ [Eq. (4)]. To estimate evaporation rate from the whole sand medium, the computed flux from Eq. (1) was multiplied by the area of wet region computed from Eq. (4) and the time interval between two scans of the column (nearly 30 min).

In addition to corner flow model (for square and triangular cross section), evaporative water loss was predicted by Buckingham-Darcy law as

$$\frac{Q}{A}=e=K(\theta)\frac{\Delta h}{\Delta z}, \tag{7}$$

with Q water volume per time flowing through sample cross section A, evaporation rate e, water content dependent hydraulic conductivity $K(\theta)$ and capillary pressure head difference Δh acting over depth interval Δz. Parametric model for macroscopic hydraulic conductivity is shown in Fig. 1(b). Figure 5 shows comparison among cumulative water loss obtained by image analysis, and predictions based on corner flow model and according to macroscopic Buckingham-Darcy law [denoted as $K(\theta)$].

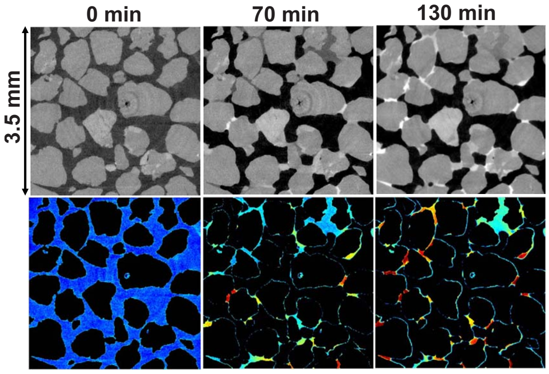

FIG. 6. (Color online) Images of phase distribution at sand surface at different times (surface defined as the cross section in which the porosity of the sand column reaches a mean value about 0.38). Black, light gray, and dark gray on top row correspond to air, solid and liquid phases, respectively (bright color indicate high salt concentrations in the liquid phase). On bottom row, the black color corresponds to both air and solid phases and other colors indicate regions differing in salt concentrations in liquid phase (bright color marks high concentration). Note that spatial distribution of higher concentrations coincides with fine pores locations, suggesting preferential flow in water-filled finer pores connected to evaporating surface.

Good agreement between measured and modeled cumulative mass loss was obtained with corner flow model assuming square capillary cross section. Results based on Buckingham-Darcy overestimated measured cumulative mass loss by nearly 3 orders of magnitude. Irrespective of the hydraulic conductivity model used, we conclude that evaporative flux supplied by capillary liquid flow was not limited by hydraulic properties of the porous medium. As expected for the experimentally induced high evaporation rate (in the range from 30 to 10 mm/day), drying rate was most likely limited by diffusive exchange across the air boundary layer above the sample surface [10,26]

C. Dynamics of salt distribution during evaporation

1. Dynamics of salt distribution at pore scale

During stage 1 evaporation (defined by continuous liquid structures) dissolved salt is convected toward evaporative surface by capillary flow. Consequently, surface salt concentration increases continuously with time enhancing the corresponding gray values of liquid phase at surface reflected with a brighter color in the recorded images as depicted in Fig. 6 (top row).

The resulting spatial distributions of liquid phase at the surface and connectivity below, shape the distribution of salt accumulation at surface (no distinction is made between dissolved and deposited salt). As shown in Fig. 6, only a few and thin liquid structures (thick films) remained continuous and supplied water to the surface resulting in spatially nonuniform evaporation pattern. These fine structures act as convective "chimneys" maintaining continuous liquid pathways to supply evaporative demand by capillary action drawing water from larger pores below toward fine pores at sand sur-

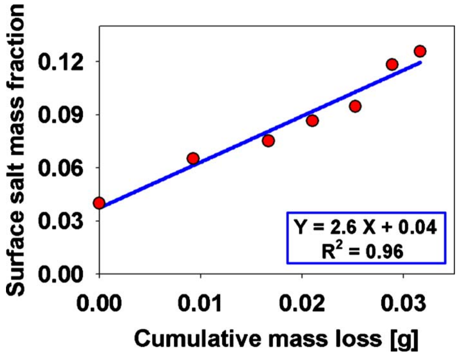

FIG. 7. (Color online) Relationship between salt mass fraction at the surface (deduced from gray values in the liquid phase) and cumulative evaporative water loss from entire sand column.

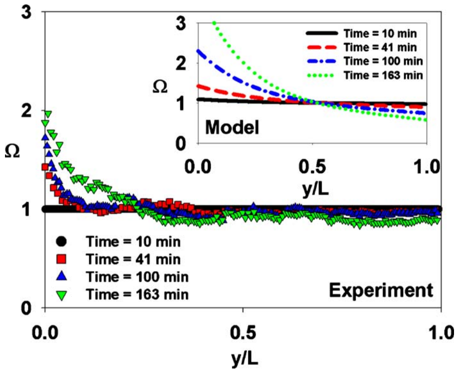

FIG. 8. (Color online) Spatial and temporal distributions of normalized salt mass fraction at different times throughout the evaporating sand column deduced from image analysis. Evaporative surface is at position $y/L=0$ with depth y and column length L. The inset shows the analytical prediction from Eq. (6).

face where vaporization increased salt concentration in these active fine pores at the surface. Figure 6 clearly shows that immediately following the onset of evaporation, large pores at surface were invaded by air; however, fine pores remained saturated acting as preferential evaporating surfaces to supply the evaporative demand.

2. Dynamics of salt distribution at macroscale

We use x-ray imagery to address the macroscopic pattern of solute concentration near the surface of an evaporating porous medium. It has been already illustrated in Fig. 6 that evaporation at surface significantly affects the dynamics of solute concentration. As a first-order approximation, we assumed linear relationship between salt mass fraction and gray value of the liquid phase which may be used to determine salt mass dynamics from gray values of liquid phase. This assumption may introduce certain error in estimation of total salt mass as gray values in 16-bit images may reach saturation (range from 0 to 65 535). For example, after the third scan, some pixels attained maximum gray value due to high amount of accumulated salt and further increase in salt mass would go undetected in those pixels (gray values may not exceed 65 535) hence resulting in underestimation of the salt mass in the image.

Figure 7 shows the temporal evolution of salt mass fraction at surface compared with the measured cumulative mass loss from the sand column postulating a linear relation between drying rate and dissolved-salt concentration. This result indicates a potential method for determining drying rate based on temporal distribution of salt concentration. By applying linear scaling between gray value and salt mass fraction for the entire column, we are able to delineate by image analysis the spatial and temporal evolution of salt mass fraction throughout the evaporating sand column as presented in Fig. 8.

A similar trend of salt distribution was observed in measurements conducted by Pel *et al.* [27] during drying of fired-clay brick with an initial value of Pe=3. According to estimates of evaporation rate determined from images, Fig. 5 indicates that between 70 and 195 min (elapsed time) evaporation rate was stable and the average evaporation rate during this period of 14 mm/day was used to compute Pe. We also used $D^*=10^{-9}\ \mathrm{m}^2\ \mathrm{s}^{-1}$ as typical value for effective diffusion coefficient of salt in water according to Huinink *et al.* [22]. The resulting Peclet number in our measurement was about 4.5. The inset in Fig. 8 shows dynamics of salt distribution predicted by the analytical solution presented in Eq. (6). Although the analytical solution proposed by Guglielmini *et al.* [12] could capture the trend of the salt distribution in our measurements, certain discrepancies between measurements and predictions remain. These deviations can be attributed to simplifying assumptions such as: constant Peclet number, constant effective diffusion coefficient (should be a function of water content), linear relationship between gray values and salt concentration, and underestimating the accumulated salt due to the experimental limitation which was explained above. Additionally, the analytical solution was proposed for the intermediate-time regime whereas in the present study it was used for the entire drying time. Nevertheless, despite several simplifying assumptions, Fig. 8 illustrates that the analytical solution provides reasonable predictions for near-surface solute concentration during evaporation.

V. SUMMARY AND CONCLUSIONS

The study confirms the often postulated role of capillary flow in supplying stage 1 evaporation. Results demonstrate that even for high evaporation rates from coarse sand under study, liquid phase continuity was maintained and hydraulic conductivity was not limiting the evaporative flux. The primary limitation to the high evaporation rate was probably limited by vapor diffusive exchange across the air boundary layer above the surface as has been demonstrated in previous studies [10,26]. The use of x-ray synchrotron radiation provided direct observations of liquid phase continuity at pore scale along the entire evaporating sand sample. Pore-scale images at high spatial resolution (7 microns) facilitated localization of preferential evaporation sites associated primarily with fine pores at the sand surface. Pore-scale imagery showed that immediately following the onset of evaporation process, large pores are invaded by air phase whereas fine pores remain saturated and act as persistent and active evaporating sites. Additional confirmation of localized evaporation sites at the surface was obtained using salt distribution dynamics and spatial patterns. Dissolved salt was transported toward the sand surface by capillary induced liquid flow mechanism and accumulated preferentially at fine pores marking the vaporization surfaces. Using the corner flow model quantitative estimate of evaporative water loss rates was in good agreement with the measured water loss computed from the x-ray images. Microscopic and sample scale solute dynamics were delineated using x-ray attenuation proportional to salt concentration, and were found to be in good agreement with the analytical solution of the convection-diffusion equation for an evaporating sample. The study provides new insights into the nature of phase continuity and dynamics near an evaporating surface which are essential for future understanding of the exact nature of limitations imparted by surface evaporating sites and diffusive boundary layer.

ACKNOWLEDGMENTS

The authors gratefully acknowledge funding by the Swiss National Science Foundation Project No. 2000021-113676/1. We thank Marco Stampanoni for his support at the Swiss Light Source of the Paul Scherrer Institute (PSI).

[1] T. M. Shaw, Phys. Rev. Lett. **59**, 1671 (1987).

[2] G. W. Scherer, J. Am. Ceram. Soc. **73**, 3 (1990).

[3] A. G. Yiotis, A. K. Stubos, A. G. Boudouvis, I. N. Tsimpanogiannis, and Y. C. Yortsos, Transp. Porous Media **58**, 63 (2005).

[4] P. Lehmann, S. Assouline, and D. Or, Phys. Rev. E **77**, 056309 (2008).

[5] N. Shokri, P. Lehmann, and D. Or, Water Resour. Res. **45**, W02415 (2009a).

[6] N. Shokri, P. Lehmann, and D. Or, Water Resour. Res. **45**, W10433 (2009b).

[7] N. Shokri, P. Lehmann, and D. Or, Geophys. Res. Lett. **35**, L19407 (2008b).

[8] I. N. Tsimpanogiannis, Y. C. Yortsos, S. Poulou, N. Kanellopoulos, and A. K. Stubos, Phys. Rev. E **59**, 4353 (1999).

[9] M. Kohout, Z. Grof, and F. Štepánek, J. Colloid Interface Sci. **299**, 342 (2006).

[10] N. Shokri, P. Lehmann, P. Vontobel, and D. Or, Water Resour. Res. **44**, W06418 (2008a).

[11] L. Xu, S. Davies, A. B. Schofield, and D. A. Weitz, Phys. Rev. Lett. **101**, 094502 (2008).

[12] L. Guglielmini, A. Gontcharov, A. J. Aldykiewicz, Jr., and H. A. Stone, Phys. Fluids **20**, 077101 (2008).

[13] D. Le, H. Hoang, and J. Mahadevan, Transp. Porous Media **80**, 229 (2009).

[14] T. D. Gonçalves, L. Pel, and J. D. Rodrigues, Environ. Geol. **52**, 293 (2007).

[15] J. Petković, H. P. Huinink, L. Pel, K. Kopinga, and R. P. J. van Hees, Mater. Struct. **40**, 475 (2007).

[16] R. Lenormand, J. Phys.: Condens. Matter **2**, SA79 (1990).

[17] M. Tuller and D. Or, Water Resour. Res. **37**, 1257 (2001).

[18] T. C. Ransohoff and C. J. Radke, J. Colloid Interface Sci. **121**, 392 (1988).

[19] J. C. T. Eijkel, B. Dan, H. W. Reemeijer, D. C. Hermes, J. G. Bomer, and A. van den Berg, Phys. Rev. Lett. **95**, 256107 (2005).

[20] M. Tuller, D. Or, and L. M. Dudley, Water Resour. Res. **35**, 1949 (1999).

[21] F. Chauvet, P. Duru, S. Geoffroy, and M. Prat, Phys. Rev. Lett. **103**, 124502 (2009).

[22] H. P. Huinink, L. Pel, and M. A. J. Michels, Phys. Fluids **14**, 1389 (2002).

[23] M. Th. van Genuchten, Soil Sci. Soc. Am. J. **44**, 892 (1980).

[24] Y. Mualem, Water Resour. Res. **12**, 513 (1976).

[25] L. A. Segura, Drying Technol. **25**, 1677 (2007).

[26] M. Suzuki and S. Maeda, J. Chem. Eng. Jpn. **1**, 26 (1968).

[27] L. Pel, H. Huinink, and K. Kopinga, Appl. Phys. Lett. **81**, 2893 (2002).